Journal of Materials Chemistry A

Accepted Manuscript

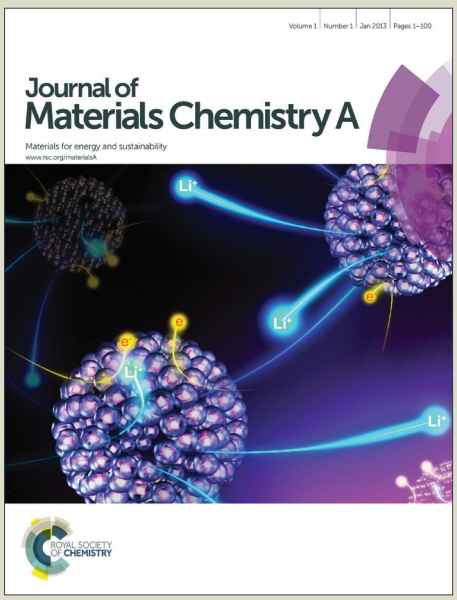

ROYAL SOCIETY OF CHEMISTRY

www.rsc.org/materialsA

Journal Name

RSCPublishing

COMMUNICATION

Ferroelectric solar cells based on inorganic–organic hybrid perovskite

Cite this: DOI: 10.1039/x0xx00000x

Bo Chen,[*a] Jian Shi,[b] Xiaojia Zheng,[*a] Yuan Zhou,[a] Kai Zhu,[c] Shashank Priya[*a]

Received 00th January 2012,
Accepted 00th January 2012

DOI: 10.1039/x0xx00000x

www.rsc.org/

Ferroelectric solar cells based on ferroelectric oxides have attracted significant attention owing to many unique advantages, such as the switchable photocurrent and photovoltage and above bandgap open circuit voltages. However, the small photocurrent densities of the typical ferroelectric solar cells greatly limit their photovoltaic performance. In this report, we experimentally revealed the polarization switching properties of inorganic–organic hybrid perovskite and developed ferroelectric solar cells based on the hybrid perovskite. Hybrid perovskite methylammonium lead trihalide ($MAPbX_3$) thin film exhibited 180° domain phase switching and polarization hysteresis loops. Ferroelectric solar cells based on the mixed halide $MAPbI_{3-x}Cl_x$ thin film demonstrate power conversion efficiency of 6.7% and the ferroelectric solar cells display switchable photovoltaic effect. This work provides an alternative but exhilarating solution for high-performance ferroelectric solar cells beyond inorganic ferroelectric oxides.

To harvest clean and renewable solar energy, in past several decades, research trend has been towards exploring novel materials and photovoltaic mechanisms to achieve higher efficiency in solar cells.[1-6] Since the discovery of photovoltaic effect in ferroelectric materials over 50 years ago,[7-9] ferroelectric solar cells (FESC) have attracted significant attention owing to many unique advantages. Different from the p-n diode or Schottky diode photovoltaic (PV) devices, whose charge separations are heavily determined by the intrinsic built-in electric fields, in the FESC, ferroelectric polarization plays a dominant role for charge separation and transport.[10-12] FESC can provide changeable directions of photocurrent and photo-voltage by polarization switching, and also generate above bandgap open circuit voltages.[13-17] These proprieties render FESC a promising candidate in solar-energy conversion. Up to now, ferroelectric solar cells based on several inorganic ferroelectric oxide thin films have been studied, including $BiFeO_3$,[18-21] $Pb(Zr,Ti)O_3$,[22-24] $BaTiO_3$,[25, 26] $(PbLa)(Zr,Ti)O_3$,[27] $KBiFe_2O_5$,[28] $[KNbO_3]_{1-x}[BaNi_{½}Nb_{½}O_{3-δ}]_x$,[29] and Bi_2FeCrO_6.[30, 31] However, the photocurrent densities under AM 1.5G solar illumination for most FESC are very small, generally on the order of $\mu A/cm^2$ or nA/cm^2, which greatly limit their photovoltaic performance with power conversion efficiency (PCE) below 2%.[10-29] The small photocurrent densities are usually ascribed to the wide band gap, poor light absorption coefficient, small charge carrier diffusion length, or low charge collection efficiency.[10-19] A breakthrough in the field of FESC occurred through the recent study on Bi_2FeCrO_6, which exhibited both small bandgap (1.4-1.6 eV) and large photocurrent density (11.7 mA/cm^2) to yield the PCE as high as 3.3%.[31] Moreover, stacking of three layer of Bi_2FeCrO_6 with different bandgaps greatly improved the PCE to 8.1%.[31] Besides the inorganic ferroelectric oxides, organic ferroelectric materials (such as P(VDF–TrFE)) have also been exploited to promote the charge separation and thereby enhancement of the PCE for solar cells.[32-35] However, substantial efforts are still needed to improve FESC's performance; more economical materials and device fabrication approaches for high efficient FESC should be developed for practical and reliable applications.

In the past five years, a new emerging class of perovskite PV materials, inorganic–organic methylammonium lead trihalide $MAPbI_{3-x}Cl_x$ and $MAPbI_3$,[36-40] have demonstrated unprecedented high power conversion efficiency due to the suitable bandgap (1.55 eV),[41-44] superior light absorption coefficient (~10^5 cm^{-1}),[45-48] and large electron/hole diffusion lengths (over 100 nm).[49-51] Interestingly, ferroelectric domains have been proposed to exist in the inorganic–organic hybrid perovskite from both experimental and computational.[52-58] Even though the space group for $MAPbI_{3-x}Cl_x$ and $MAPbI_3$ is centrosymmetric tetragonal I4/mcm,[53] the orientational order of $CH_3NH_3^+$ dipoles can influence the magnitude of bulk polarization,[56, 57] as a result, the molecular $CH_3NH_3^+$ dipoles can reduce the lattice symmetry to quasi I4cm with noncentrosymmetric structure and have ferroelectric properties.[56] Rappe *et al.* reported a strong bulk polarization in $MAPbI_{3-x}Cl_x$ and $MAPbI_3$ from first-principles density functional theory calculations, and they further explored the energies and electronic structures of domain walls in $MAPbI_{3-x}Cl_x$, $MAPbI_3$ and $MAPbBr_3$ thin films.[57, 58] Padture *et al.* experimentally observed the ferroelectric domain in the $MAPbI_3$ perovskite thin films by piezoresponse force microscopy.[52] This ferroelectric effect offers the opportunity for tuning and utilizing the polarization electric field in inorganic–organic hybrid perovskite for improving the performance of the FESC.

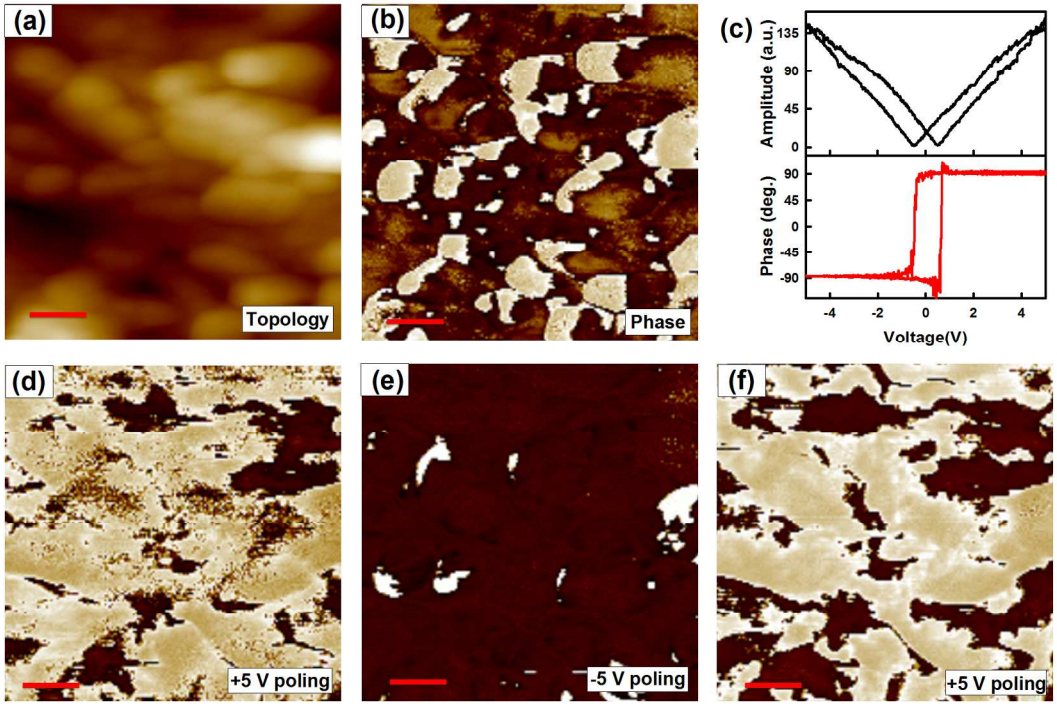

Fig. 1 (a) PFM topology and (b) PFM phase image of as-grown $MAPbI_{3-x}Cl_x$ thin film. (c) Piezoresponse amplitude and piezoresponse phase at different bias voltages. (d), (e), and (f) is the PFM phase image after electric poling of the sample at +5V, -5V, and +5V, respectively, and the corresponding topology is shown in Fig. S2. The scale bar is 200 nm.

In this report, we study the ferroelectric switching properties of methylammonium lead trihalide ($MAPbX_3$) thin film and propose the ferroelectric solar cells based on the inorganic–organic $MAPbX_3$ perovskite. Both $MAPbI_{3-x}Cl_x$, $MAPbI_3$ and $MAPbBr_3$ thin films exhibited 180° domain phase switching and polarization hysteresis loops. The polarization states of the ferroelectric methylammonium lead trihalide light absorber show closely relate to the open circuit voltage, photocurrent and eventually affect the power conversion efficiency of the FESCs. The ferroelectric solar cells based on $TiO_2/MAPbI_{3-x}Cl_x/Au$ structure demonstrated power conversion efficiency of 6.7%. Symmetrical switchable PV effect was achieved from symmetric FESC with $Au/MAPbX_3/Au$ configuration.

Ferroelectric effect of the mixed halide $MAPbI_{3-x}Cl_x$ thin film was first investigated by piezoresponse force microscopy (PFM). When a biased alternating voltage is applied to the sample surface, the piezoelectric sample will respond by either volume expansion or contraction according to the converse piezoelectric effect. This response can be used to map out the piezoelectric phase (domain configuration) and amplitude (piezoelectric response) of the specimen accordingly. We investigated the piezoelectric nature of as-grown $MAPbI_{3-x}Cl_x$ thin film with thickness of ~250 nm (**Fig. 1**). The PFM phase image clearly demonstrates the strong contrast with bright/dark area, indicating upward/downward oriented domains (Fig. 1b). This observation indicates the existence of significant magnitude of spontaneous polarization across the as-grown $MAPbI_{3-x}Cl_x$ thin films.

To further investigate the polarization switching behavior, positive and negative DC voltage was applied alternatively across the sample prior to the piezoresponse phase mapping, as shown in Fig. 1d~f. After electric poling at +5 V DC bias voltage, most of the domains aligned upwards (Fig. 1d). An obvious switching of domain direction was observed after further poling at -5 V bias voltage. Subsequently, the sample was again poled with +5 V, and the dominant domains switched back to upward direction, indicating the reversibility and repeatability of electric-field-induced polarization. In order to better quantify the switching capability, the sample was poled at selected locations on the film surface by applying DC tip bias during scanning, as shown in Fig. 1c. A sharp 180° phase change in the PFM phase coupled with the dip in the PFM amplitude occurs at coercive voltage (V_C) with magnitude of ± 0.5 V. This indicates that the coercive field for $MAPbI_{3-x}Cl_x$ perovskite is ~20 kV/cm. The observation of clear hysteresis loops suggests that the material is highly polarizable and the ferroelectric domains can be switched through external applied field. The bulk hysteresis was also measured by polarization-electric field loop on $Au/MAPbI_{3-x}Cl_x/Au$ structure (Fig. S3), and it demonstrated leakage characteristic, which might due to the relatively high conductivity of the organometal perovskite. This typical effect of leakage current has also been observed in other ferroelectric solar cells.[21, 22]

Building upon the PFM studies, we propose a ferroelectric photovoltaic device based on $MAPbI_{3-x}Cl_x$ thin film with configuration: $TiO_2/FE/Au$, where *FE* denotes $MAPbI_{3-x}Cl_x$ (**Fig. 2**). When the *FE* layer is in its pristine state (Fig. 2a), due to the work function mismatch between *FE* and Au, it forms a Schottky barrier diode at *FE*/Au interface. On the other side, compact TiO_2 thin layer serves as *n*-type electron-transport layer (ETL), and a narrow *n-FE* junction is created at the TiO_2/FE interface with smaller work function mismatch than *FE*/Au interface. It should be noted that *FE* layer shows strong semiconducting property, which was recently revealed by the electron beam-induced current measurement.[59] Under light illumination, the TiO_2/pristine-*FE*/Au structure would demonstrate a PV behavior. The open circuit voltage (V_{OC}) would be representative of the intrinsic built-in electric filed (E_{bi}) from both the Schottky diode and the *n-FE* junction. Ferroelectric polarization

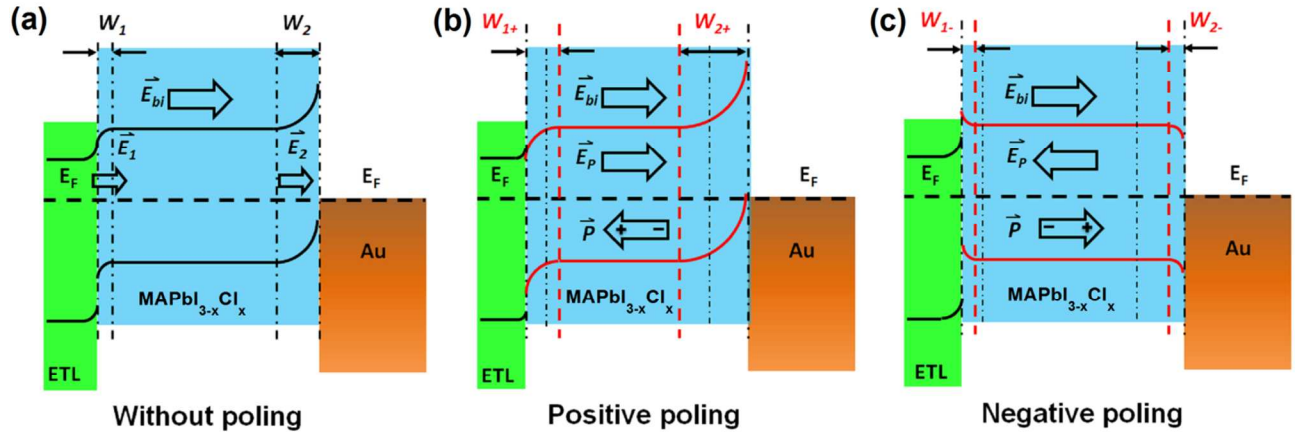

Fig. 2. Schematics of electronic band structure for ferroelectric solar cell based on $MAPbI_{3-x}Cl_x$ under different polarization conditions: (a) without poling, (b) after positive poling, and (c) after negative poling.

electric field (E_P) can change the width of the depletion regions inside the *FE* layer, which would be expected to regulate the separation of photo-generated charges.

When FE is positively poled (ETL side is grounded), negative ferroelectric charges appear in the FE layer on the Au side and positive charges appear on the ETL side. Such ferroelectric polarization leads to the increase of the width of depletion regions in the *FE* layer (W_{1+} and W_{2+}) and enlarges the band bending at both *FE*/Au and *n*/*FE* interfaces (Fig. 2b). As a result, a boosting of V_{OC} and J_{sc} would be observed due to additional band bending and better charge separation. And a higher PV efficiency is expected without introducing any extra layer such as the expensive hole-transport layer (e.g. Spiro-OMeTAD)![36-40] When the *FE* layer is negatively poled as shown in Fig. 2c, the band bending at both interfaces would be reduced and even reversed if large enough polarization is developed. Considering that the driving force for charge separation comes from both E_{bi} and E_P, for a first-order approximation, we have:

$$V_{OC+} = V_{bi} + V_p \quad (1)$$

$$V_{OC-} = V_{bi} - V_p \quad (2)$$

where V_{OC+} and V_{OC-} is the open circuit voltage for FESC after positive poling and negative poling, respectively; V_{bi} represents the overall band bending potential in the *FE* layer due to built-in electric field at both interfaces; V_p comes from the switchable polarization component. If E_P is larger than E_{bi} at an interface, reverse band bending would occur at this interface leading to a switching of the PV diode polarity. Apparently, a substantial V_p, being the major driving force for charge separation in such FESC, would dictate the absolute value of energy conversion efficiency.

Following the concept described in Fig. 2, we experimentally proceed to the FESC device as shown in **Fig. 3**. The device was composed of a 60 nm compact TiO_2 (cp-TiO_2) layer, a 250 nm ferroelectric $MAPbI_{3-x}Cl_x$ light absorber and 100 nm Au top electrode. The corresponding photovoltaic performance of the FESC under different polarization conditions is shown in Fig. 3b. The performance of the solar cell based on as-grown $MAPbI_{3-x}Cl_x$ thin film exhibited poor PV performance with V_{OC} = 0.37 V, J_{SC} = 1.47 mA/cm^2, *FF* = 16.94%, and *PCE* = 0.09%. After conducting +2 V poling process, the photovoltaic performance was significantly enhanced to 6.7%. The V_{OC} was increased to 0.72 V, J_{SC} jumped to 18.53 mA/cm^2, and *FF* was increased to 50.24%. The increase of PCE by 74 times and increase of J_{SC} by 12 times after positive poling suggests the absolutely dominant role of polarization electric field in $MAPbI_{3-x}Cl_x$ in enabling efficient charge separation and transport. On the other hand, the photovoltaic performance was greatly suppressed after -2 V negative poling of the device, where the V_{OC} is switched to a negative value (-0.12 V). These observations

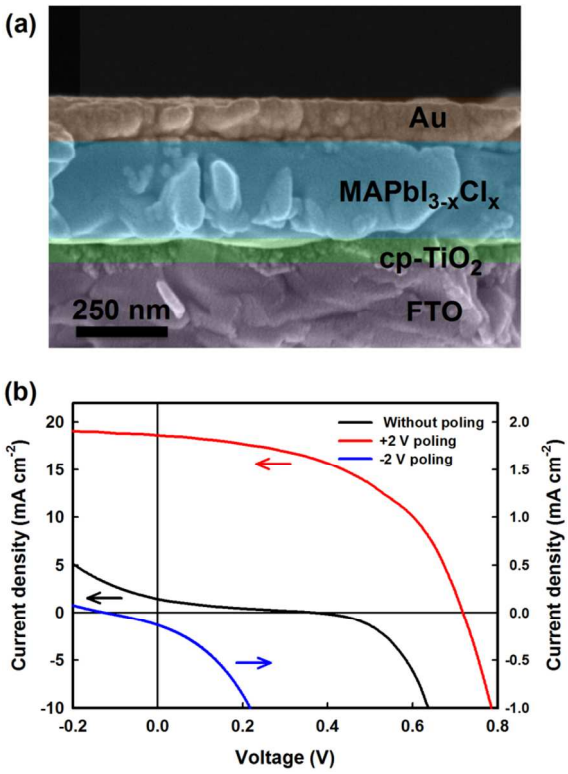

Fig. 3. (a) SEM image and (b) *J*-*V* plots of the ferroelectric solar cell with TiO_2/$MAPbI_{3-x}Cl_x$/Au structure.

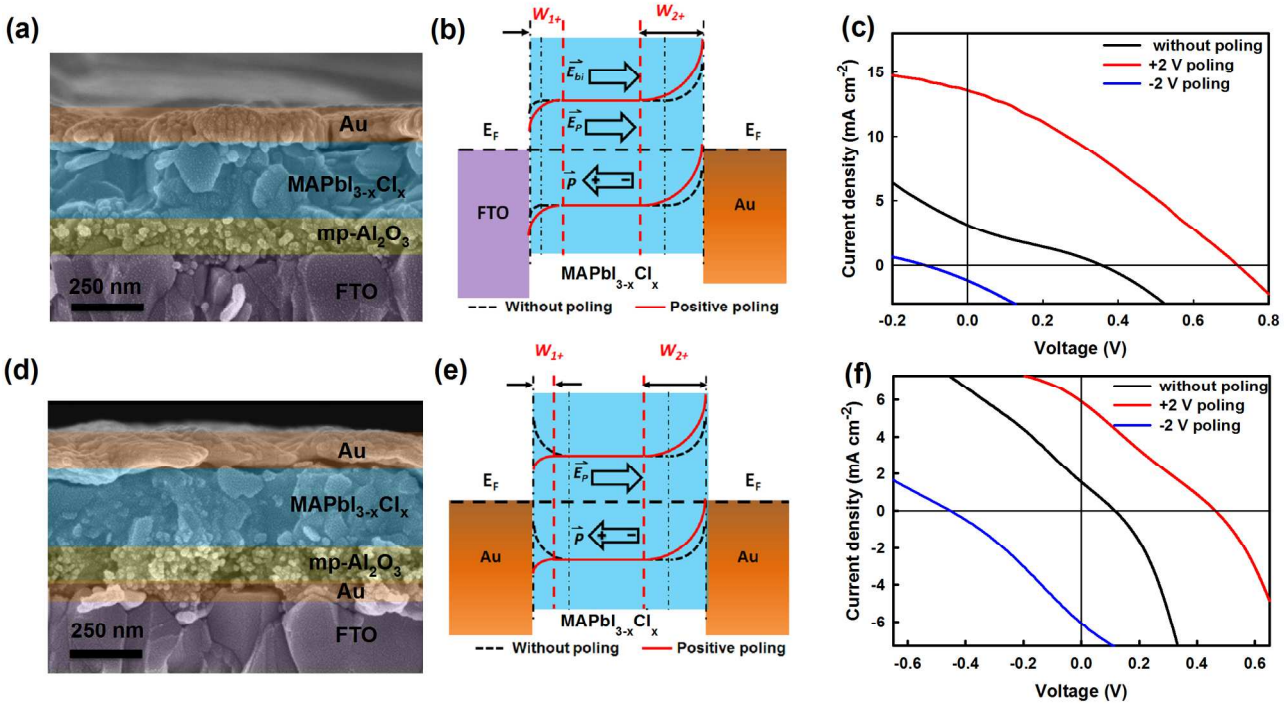

Fig. 4. (a) SEM image, (b) band diagram, (c) *J-V* plots of the *FESC* with FTO/mp-Al_2O_3/$MAPbI_{3-x}Cl_x$/Au structure. (d) SEM image, (e) band diagram, (f) *J-V* plots of the *FESC* with FTO/Au/mp-Al_2O_3/$MAPbI_{3-x}Cl_x$/Au structure.

match with our proposed mechanism in Fig. 2. According to the given equations (1) and (2), 0.84 V difference of V_{OC} between the positively poled and negatively poled *FESC* gives rise to V_P of 0.42 V, which is consistent with the coercive voltage (V_C ~0.5 V) for polarization switching.

For an ideal FESC that operates only based on the polarization electric field, both of its photocurrent and photo-voltage should be switchable and exhibit symmetry behavior through zero. Though we did observe that the output current and voltage could be switched in the solar cell mentioned above, they were not symmetrical. This can be simply explained by the asymmetric structure of the FESC device described here. Based upon this understanding, we designed two more cell structures (FTO/$MAPbI_{3-x}Cl_x$/Au and Au/$MAPbI_{3-x}Cl_x$/Au) to demonstrate the tuning capability of the electrodes on the symmetry of the J-V characteristics in the FESC.

FTO/$MAPbI_{3-x}Cl_x$/Au structure was proposed for the FESC with electrode/*FE*/electrode configuration. Due to the incomplete surface coverage of $MAPbI_{3-x}Cl_x$ thin film on FTO/glass substrate,[36, 44, 60] the top Au electrode can make direct contact with the bottom FTO electrode for FESC device, which could short circuit the cell and screen the photovoltaic effect. To avoid this problem, we introduced a 125 nm mesoporous-Al_2O_3 layer (mp-Al_2O_3) between FTO and $MAPbI_{3-x}Cl_x$ to develop high coverage $MAPbI_{3-x}Cl_x$ film on FTO substrate.[44] The ferroelectric film first fills the mp-Al_2O_3 layer and the excess $MAPbI_{3-x}Cl_x$ forms a 210 nm capping layer on top of mp-Al_2O_3 as shown in **Fig. 4**a. The band diagram for FESC based on the insulating mp-Al_2O_3 for FTO/$MAPbI_{3-x}Cl_x$/Au cell is shown in Fig. S6. FTO is a highly doped n-type semiconductor and has similar Femi level as TiO_2. Therefore, similar to that of the TiO_2/*FE*/Au structure, band bending in $MAPbI_{3-x}Cl_x$ on the FTO side is a *n-FE* structure and band bending on Au side is a Schottky barrier for pristine *FE* state (Fig. S6a or dashed line in Fig. 4b). The as-grown FESC on mp-Al_2O_3 shows small photovoltaic performance with V_{OC} equal to 0.35 V (Fig. 4c). After positive poling, band bending should become enhanced at both ends with large depletion regions (red line in Fig. 4b), and a better PV performance was achieved with V_{OC+} value of 0.72 V. Negative poling leads to alignment of domains that negates the built-in field (Fig. S6c). Most *FE* polarization should be used to counter the original band bending and the leftover (if there is) finally reverse the band bending at both interfaces. Indeed, experimentaly the V_{OC-} value under negative poiling case is only -0.11 V. The difference between V_{OC+} and V_{OC-} leads to V_p = 0.415 V and V_{bi} = 0.305 V for FESC with FTO/mp-Al_2O_3/$MAPbI_{3-x}Cl_x$/Au structure. This structure perfectly reproduces our findings in the TiO_2/FE/Au device and its PV behavior is consistent with our concept. The asymmetric J-V characteristics arise from the asymmetric structure and their associated asymmetric band bending.

For the development of a symmetric FESC, we fabricated a FESC device based on the Au/$MAPbI_{3-x}Cl_x$/Au configuration. Between the mp-Al_2O_3 and FTO substrate, a 30 nm Au thin film was added to serve as the bottom electrode; the stack structure of FESC is thus FTO/Au/mp-Al_2O_3/$MAPbI_{3-x}Cl_x$/Au (Fig. 4d). According to our previous model, different from the FESC structures in Fig. 3a and 4a, the Au/*FE*/Au would yield a symmetric PV diode performance. Without poling, the Au/*FE*/Au has symmetric Schottky barrier on both sides (dashed line in Fig. 4e or Fig. S7a), which will cancel each other out and show negligible effect on the whole device. When *FE* is positively poled, the left-side band bending in *FE* would be reduced and even reversed, whereas the right-side band bending would be enhanced (red line in Fig. 4e or Fig. S7b). Overall, we have a possible Ohmic contact on the left side and an enhanced Schottky contact on the right side. Similarly, when FE is negatively poled, the left side forms a stronger Schottky contact and the right side forms a possible Ohmic contact, and we expect a similar performance to that under positive poling. Experimentally, as shown in Fig. 4f, the FESC demonstrated switchable photovoltaic effect: V_{OC} is 0.44 V and J_{SC} is 5.90 mA/cm^2 under positive poling; V_{OC} is -0.45 V and J_{SC} is -5.71 mA/cm^2 under negative poling. These observations align exactly with our hypothesis. Due to the semi-transparent properties of the thin Au film, the light intensity is reduced after passing through the Au bottom electrode, which leads

to smaller J_{SC} value. ΔV_{OC} under positive poling and negative poling is 0.89 V, which is also consistent with the difference of coercive voltage for polarization switching. The small V_{OC} value for the FESC before poling may be due to the spontaneous polarization for the as-grown $MAPbI_{3-x}Cl_x$ thin film. We studied the switchable ferroelectric PV performance for $MAPbI_{3-x}Cl_x$ solar cells under alternative positive and negative electric poling for many times, and the result in Fig. S4 demonstrate the repeatable photovoltaic response after positive and negative poling.

Besides the $MAPbI_{3-x}Cl_x$, we also investigated the ferroelectric properties and the performance of corresponding symmetric FESC for $MAPbI_3$ and $MAPbBr_3$. As shown in Fig. S8 and S9, both the as-grown 250 nm $MAPbI_3$ and $MAPbBr_3$ thin films demonstrate strong domain contrast with bright and dark area in the PFM phase image. Hysteresis loops in PFM phase response at different bias voltage reveal 180° phase switching with coercive voltage at ± 0.2 V and ± 0.37 V for $MAPbI_3$ and $MAPbBr_3$ thin film, respectively. This indicates the ferroelectric effect is a common property for the methylammonium lead trihalide ($MAPbX_3$). The coercive field for $MAPbI_3$ is ~8 kV/cm, which is about half for the ferroelectric $MAPbI_{3-x}Cl_x$ perovskite. This might be ascribed to the doping effect of the chloride, but the detail reason is still not sure. For the performance of symmetric FESC devices based on $Au/MAPbI_3/Au$ (Fig. S10) and $Au/MAPbBr_3/Au$ configurations (Fig. S11), switchable J-V curves are also observed. The value of ΔV_{OC} for $MAPbI_3$ and $MAPbBr_3$ is 0.38 V and 0.66 V, respectively, which is consistent with its coercive voltage.

As shown above, a new prototype of the ferroelectric solar cells based on the inorganic–organic hybrid perovskite has been proposed and realized in this paper. Considering the excellent PV performance of the hybrid perovskite has been demonstrated in the hybrid perovskite solar cells with hole-transport material and electron-collecting layer,[36-44] the ferroelectric properties of the hybrid perovskite thin film will bring us a whole new device design to fabricate high-efficiency FESC. The inorganic–organic hybrid perovskite can provide light absorbers with diverse bandgaps ranging from 1.17 eV to 2.28 eV by changing A, B or X in the perovskite ABX_3 structure.[61-65] This tunable bandgap enables convenient engineering of the FESC structure in the future, and also provides the potential to stack multilayer of hybrid perovskites to increase light absorption and reduce thermalization loss. Moreover, inorganic–organic hybrid perovskite can achieve crystalline structure by simply precipitating out of the solution followed by low-temperature annealing, which avoids the use of expensive growth techniques for the FESC device.

Conclusions

In summary, we investigate the ferroelectric properties of the methylammonium lead trihalide thin films, and develop a new type of ferroelectric solar cell based on this inorganic–organic hybrid perovskites. The FESC based on $TiO_2/MAPbI_{3-x}Cl_x/Au$ structure demonstrated the power conversion efficiency as high as 6.7%, which is a large breakthrough with respect to the FESC based on inorganic ferroelectric oxide. Moreover, for the symmetric FESC structure, both of the directions of the output voltage and output current can be switched by change the polarization direction of the ferroelectric $MAPbX_3$ thin film. We also find that the open circuit voltage difference between positive-poled and negative-poled FESC is dependent upon the coercive voltage of the selected materials. Due to the excellent PV properties of the inorganic–organic hybrid perovskite, ferroelectric inorganic–organic hybrid materials open a new and promising avenue to develop efficient FESC.

Acknowledgement:

The authors gratefully acknowledge the financial support through US Army under contract No.W15P7T-13-C-A910. The work at the National Renewable Energy Laboratory was supported by the U.S. Department of Energy under Contract No. DE-AC36-08-GO28308. K.Z. acknowledges the support by the U.S. Department of Energy (DOE) SunShot Initiative under the Next Generation Photovoltaics 3 program (DE-FOA-0000990).

Notes and references

[a] Center for Energy Harvesting Materials and System, Virginia Tech, Blacksburg, Virginia 24061, United States

[b] Department of Materials Science and Engineering, Rensselaer Polytechnic Institute, Troy, New York 12180, United States.

[c] Chemical and Nanoscience Center, National Renewable Energy Laboratory, Golden, Colorado 80401, United States.

† Corresponding author: bochen09@vt.edu, xiaojia@vt.edu, spriya@vt.edu.

Electronic Supplementary Information (ESI) available: Experimental details and characterization are included. See DOI: 10.1039/c000000x/

1. B. Oregan and M. Grätzel, *Nature*, 1991, **353**, 737-740.
2. T. Choi, S. Lee, Y. J. Choi, V. Kiryukhin and S. W. Cheong, *Science*, 2009, **324**, 63-66.
3. J. Y. Kim, K. Lee, N. E. Coates, D. Moses, T. Q. Nguyen, M. Dante and A. J. Heeger, *Science*, 2007, **317**, 222-225.
4. W. A. Tisdale, K. J. Williams, B. A. Timp, D. J. Norris, E. S. Aydil and X. Y. Zhu, *Science*, 2010, **328**, 1543-1547.
5. C. N. Eisler, Z. e. R. Abrams, M. T. Sheldon, X. Zhang and H. A. Atwater, *Energy Environ. Sci.*, 2014, **7**, 3600-3605.
6. A. Pandey and P. Guyot-Sionnest, *Science*, 2008, **322**, 929-932.
7. A. G. Chynoweth, *Phys. Rev. B*, 1956, **102**, 705-714.
8. A. M. Glass, D. V. D. Linde and T. J. Negran, *Appl. Phys. Lett.*, 1974, **25**, 233-235.
9. V. M. Fridkin, *Photoferroelectrics*, Springer, 1979.
10. M. Qin, K. Yao and Y. C. Liang, *Appl. Phys. Lett.*, 2008, **93**.
11. J. Kreisel, M. Alexe and P. A. Thomas, *Nat. Mater.*, 2012, **11**, 260-260.
12. Y. Yuan, Z. Xiao, B. Yang and J. Huang, *J. Mater. Chem. A*, 2014, **2**, 6027-6041.
13. W. Ji, K. Yao and Y. C. Liang, *Adv. Mater.*, 2010, **22**, 1763-1766.
14. R. K. Katiyar, P. Misra, F. Mendoza, G. Morell and R. S. Katiyar, *Appl. Phys. Lett.*, 2014, **105**.
15. S. Y. Yang, J. Seidel, S. J. Byrnes, P. Shafer, C. H. Yang, M. D. Rossell, P. Yu, Y. H. Chu, J. F. Scott, J. W. Ager, III, L. W. Martin and R. Ramesh, *Nat. Nanotech.*, 2010, **5**, 143-147.
16. A. Bhatnagar, A. R. Chaudhuri, Y. H. Kim, D. Hesse and M. Alexe, *Nat. Commun.*, 2013, **4**.
17. M. Alexe and D. Hesse, *Nat. Commun.*, 2011, **2**.
18. W.-M. Lee, J. H. Sung, K. Chu, X. Moya, D. Lee, C.-J. Kim, N. D. Mathur, S. W. Cheong, C. H. Yang and M.-H. Jo, *Adv. Mater.*, 2012, **24**, OP49-OP53.
19. R. Moubah, O. Rousseau, D. Colson, A. Artemenko, M. Maglione and M. Viret, *Adv. Funct. Mater.*, 2012, **22**, 4814-4818.
20. P. Zhao, L. Bian, L. Wang, J. Xu and A. Chang, *Appl. Phys. Lett.*, 2014, **105**.

21. S. Y. Yang, L. W. Martin, S. J. Byrnes, T. E. Conry, S. R. Basu, D. Paran, L. Reichertz, J. Ihlefeld, C. Adamo, A. Melville, Y. H. Chu, C. H. Yang, J. L. Musfeldt, D. G. Schlom, J. W. Ager and R. Ramesh, *Appl. Phys. Lett.*, 2009, **95**, 062909.
22. D. Cao, C. Wang, F. Zheng, W. Dong, L. Fang and M. Shen, *Nano Lett.*, 2012, **12**, 2803-2809.
23. F. Zheng, Y. Xin, W. Huang, J. Zhang, X. Wang, M. Shen, W. Dong, L. Fang, Y. Bai, X. Shen and J. Hao, *J. Mater. Chem. A*, 2014, **2**, 1363.
24. F. Zheng, P. Zhang, X. Wang, W. Huang, J. Zhang, M. Shen, W. Dong, L. Fang, Y. Bai, X. Shen, H. Sun and J. Hao, *Nanoscale*, 2014, **6**, 2915-2921.
25. C. J. Won, Y. A. Park, K. D. Lee, H. Y. Ryu and N. Hur, *J. Appl. Phys.*, 2011, **109**, 084108.
26. A. Zenkevich, Y. Matveyev, K. Maksimova, R. Gaynutdinov, A. Tolstikhina and V. Fridkin, *Phys. Rev. B*, 2014, **90**.
27. J. Zhang, X. Su, M. Shen, Z. Dai, L. Zhang, X. He, W. Cheng, M. Cao and G. Zou, *Sci. Rep.*, 2013, **3**, 2109.
28. G. Zhang, H. Wu, G. Li, Q. Huang, C. Yang, F. Huang, F. Liao and J. Lin, *Sci. Rep.*, 2013, **3**, 1265.
29. I. Grinberg, D. V. West, M. Torres, G. Gou, D. M. Stein, L. Wu, G. Chen, E. M. Gallo, A. R. Akbashev, P. K. Davies, J. E. Spanier and A. M. Rappe, *Nature*, 2013, **503**, 509-512.
30. R. Nechache, C. Harnagea, S. Licoccia, E. Traversa, A. Ruediger, A. Pignolet and F. Rosei, *Appl. Phys. Lett.*, 2011, **98**, 202902.
31. R. Nechache, C. Harnagea, S. Li, L. Cardenas, W. Huang, J. Chakrabartty and F. Rosei, *Nat. Photonics*, 2014, DOI: 10.1038/NPHOTON.2014.1255.
32. L. Hu, S. Dalgleish, M. M. Matsushita, H. Yoshikawa and K. Awaga, *Nat. Commun.*, 2014, **5**.
33. Y. Yuan, P. Sharma, Z. Xiao, S. Poddar, A. Gruverman, S. Ducharme and J. Huang, *Energy Environ. Sci.*, 2012, **5**, 8558-8563.
34. Y. B. Yuan, T. J. Reece, P. Sharma, S. Poddar, S. Ducharme, A. Gruverman, Y. Yang and J. S. Huang, *Nat. Mater.*, 2011, **10**, 296-302.
35. K. S. Nalwa, J. A. Carr, R. C. Mahadevapuram, H. K. Kodali, S. Bose, Y. Q. Chen, J. W. Petrich, B. Ganapathysubramanian and S. Chaudhary, *Energy Environ. Sci.*, 2012, **5**, 7042-7049.
36. M. Z. Liu, M. B. Johnston and H. J. Snaith, *Nature*, 2013, **501**, 395-+.
37. J. Burschka, N. Pellet, S. J. Moon, R. Humphry-Baker, P. Gao, M. K. Nazeeruddin and M. Grätzel, *Nature*, 2013, **499**, 316-+.
38. B. Conings, L. Baeten, C. De Dobbelaere, J. D'Haen, J. Manca and H. G. Boyen, *Adv. Mater.*, 2014, **26**, 2041-2046.
39. P. W. Liang, C. Y. Liao, C. C. Chueh, F. Zuo, S. T. Williams, X. K. Xin, J. J. Lin and A. K. Y. Jen, *Adv. Mater.*, 2014, **26**, 3748-3754.
40. M. Xiao, F. Huang, W. Huang, Y. Dkhissi, Y. Zhu, J. Etheridge, A. Gray-Weale, U. Bach, Y.-B. Cheng and L. Spiccia, *Angew. Chem.*, 2014, **126**, 10056-10061.
41. M. M. Lee, J. Teuscher, T. Miyasaka, T. N. Murakami and H. J. Snaith, *Science*, 2012, **338**, 643-647.
42. M. Grätzel, *Nat. Mater.*, 2014, **13**, 838-842.
43. H. P. Zhou, Q. Chen, G. Li, S. Luo, T. B. Song, H. S. Duan, Z. R. Hong, J. B. You, Y. S. Liu and Y. Yang, *Science*, 2014, **345**, 542-546.
44. G. E. Eperon, V. M. Burlakov, P. Docampo, A. Goriely and H. J. Snaith, *Adv. Funct. Mater.*, 2014, **24**, 151-157.
45. N. J. Jeon, J. H. Noh, Y. C. Kim, W. S. Yang, S. Ryu and S. Il Seol, *Nat. Mater.*, 2014, **13**, 897-903.
46. T. C. Sum and N. Mathews, *Energy Environ. Sci.*, 2014, **7**, 2518-2534.
47. S. Sun, T. Salim, N. Mathews, M. Duchamp, C. Boothroyd, G. Xing, T. C. Sum and Y. M. Lam, *Energy Environ. Sci.*, 2014, **7**, 399.
48. W. J. Yin, T. T. Shi and Y. F. Yan, *Adv. Mater.*, 2014, **26**, 4653-+.
49. S. D. Stranks, G. E. Eperon, G. Grancini, C. Menelaou, M. J. Alcocer, T. Leijtens, L. M. Herz, A. Petrozza and H. J. Snaith, *Science*, 2013, **342**, 341-344.
50. G. Xing, N. Mathews, S. Sun, S. S. Lim, Y. M. Lam, M. Gräetzel, S. Mhaisalkar and T. C. Sum, *Science*, 2013, **342**, 344-347.
51. Z. Xiao, Q. Dong, C. Bi, Y. Shao, Y. Yuan and J. Huang, *Adv. Mater.*, 2014, **26**, 6503-6509.
52. Y. Kutes, L. H. Ye, Y. Y. Zhou, S. P. Pang, B. D. Huey and N. P. Padture, *J. Phys. Chem. Lett.*, 2014, 3335-3339.
53. C. C. Stoumpos, C. D. Malliakas and M. G. Kanatzidis, *Inorg. Chem.*, 2013, **52**, 9019-9038.
54. H.-Y. Ye, Y. Zhang, D.-W. Fu and R.-G. Xiong, *Angew. Chem. Int. Ed.*, 2014, **53**, 11242-11247.
55. A. Stroppa, D. Di Sante, P. Barone, M. Bokdam, G. Kresse, C. Franchini, M. H. Whangbo and S. Picozzi, *Nat. Commun.*, 2014, **5**, 5900.
56. C. Quarti, E. Mosconi and F. De Angelis, *Chem. Mater.*, 2014, **26**, 6557-6569.
57. F. Zheng, H. Takenaka, F. G. Wang, N. Z. Koocher and A. M. Rappe, *J. Phys. Chem. Lett.*, 2015, **6**, 31−37.
58. S. Liu, F. Zheng, N. Z. Koocher, H. Takenaka, F. Wang and A. M. Rappe, *J. Phys. Chem. Lett.*, 2015, **6**, 693-699.
59. E. Edri, S. Kirmayer, S. Mukhopadhyay, K. Gartsman, G. Hodes and D. Cahen, *Nat. Commun.*, 2014, **5**, 3461.
60. B. Conings, L. Baeten, C. De Dobbelaere, J. D'Haen, J. Manca and H. G. Boyen, *Adv. Mater.*, 2014, **26**, 2041-2046.
61. B. Cai, Y. Xing, Z. Yang, W.-H. Zhang and J. Qiu, *Energy Environ. Sci.*, 2013, **6**, 1480-1485.
62. J. H. Noh, S. H. Im, J. H. Heo, T. N. Mandal and S. I. Seok, *Nano Lett.*, 2013, **13**, 1764-1769.
63. F. Hao, C. C. Stoumpos, D. H. Cao, R. P. H. Chang and M. G. Kanatzidis, *Nat. Photonics*, 2014, **8**, 489-494.
64. A. Mei, X. Li, L. Liu, Z. Ku, T. Liu, Y. Rong, M. Xu, M. Hu, J. Chen, Y. Yang, M. Grätzel and H. W. Han, *Science*, 2014, **345**, 295-298.
65. J. W. Lee, D. J. Seol, A. N. Cho and N. G. Park, *Adv. Mater.*, 2014, **26**, 4991-4998.

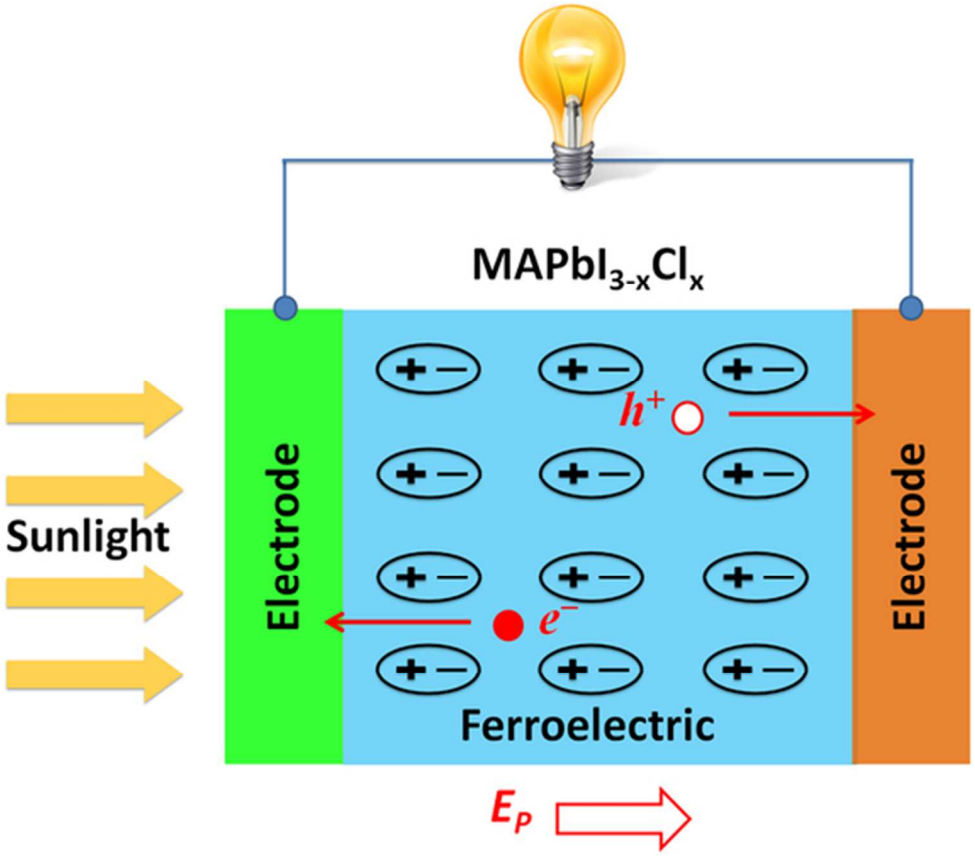

Graphical Abstract
49x43mm (300 x 300 DPI)